This is the peer reviewed author accepted manuscript (post print) version of a published work that appeared in final form in:

Lashkari, Ali, Shourijeh, Piltan Tabatabaie, Khorasani, Seyed Saeid Sahebkar, Irani, Nazanin, Rahman, Md Mizanur 2022 'Effects of over-consolidation history on flow instability of clean and silty sands', Acta Geotechnica, online, pp. 1-19

This un-copyedited output may not exactly replicate the final published authoritative version for which the publisher owns copyright. It is not the copy of record. This output may be used for non-commercial purposes.

The final definitive published version (version of record) is available at:
https://doi.org/10.1007/s11440-022-01502-y

Persistent link to the UniSA Research Outputs Repository:
https://researchoutputs.unisa.edu.au/11541.2/28898

General Rights

Copyright and moral rights for the publications made accessible in the UniSA Research Outputs Repository are retained by the authors and/or other copyright owners and it is a condition of accessing publications that users recognize and abide by the legal requirements associated with these rights.

- Users may download and print one copy for the purpose of private study or research.
- You may not further distribute the material or use it for any profit-making activity or commercial gain
- You may freely distribute the persistent link identifying the publication in the UniSA Research Outputs Repository

If you believe that this document breaches copyright, please contact us and provide details. We will remove access to the work immediately and investigate your claim.

Effects of over-consolidation history on flow instability of clean and silty sands

Abstract
This article presents an experimental program under the constant volume condition to investigate the influence of over-consolidation on flow instability of clean and silty sand specimens prepared by a systematic increase of fines contents, where fines are particles smaller than 0.075 mm of non-plastic minerals. An extensive series of constant volume Direct Simple Shear (DSS) tests on normally- and over-consolidated clean and silty Firoozkuh No. 161 sand specimens were carried out. The testing program covers a range of initial void ratios, effective vertical stresses, and fines contents. Analysis of the laboratory data indicates that over-consolidation history leads to an increase in the slope of the instability line and a rise in normalized constant volume shear strength at the onset of flow instability. Furthermore, at the same normalized constant volume shear strength, brittleness index and maximum excess pore-water pressure ratio increase with over-consolidation. Even though an increase in fines content leads to a family of non-unique critical state lines in the shear stress versus effective vertical stress plane, it is observed that the slope of the instability line and normalized constant volume shear strength vary almost uniquely with state parameter are at the onset of flow instability irrespective of fines content.

Keywords: Sand; critical state; Over-Consolidation Ratio (OCR); Instability Line (IL); state parameter; direct simple shear test

1. Introduction

The term instability is generally attributed to the quick generation of large permanent deformations due to the inability of soil internal load-bearing microstructure to withstand certain combinations of external loads and displacements (e.g., Chu et al., 2012; Wanatowski & Chu, 2012). Flow instability, a particular type of instability in loose granular soils which commonly occurs under the undrained (say constant volume) condition, is responsible for many geotechnical hazards, including landslides, failure of slopes, and collapse of mine waste tailing dams (e.g., Sladen et al., 1985; Lade, 1992; Ishihara, 1993; Chu & Leong, 2001; Chu et al., 2003; Lade & Yamamuro, 2011; Yang & Wei, 2012; Wei & Yang, 2014; Sadrekarimi 2014; Monkul et al., 2015; Wijewickreme & Soysa, 2016; Hubler et al., 2017; Lashkari et al., 2017; Yang & Luo, 2018; Zhang & Askarinejad, 2019; Song & Sun, 2019; Lashkari et al., 2020; Wei et al., 2020; Sadrekarimi, 2020; Sadrekarimi & Riveros, 2020). Flow instability is normally sudden, and the instantaneous transition from quasi-static to fully dynamic regime of deformation is accompanied by a chaotic displacement field without any localized pattern. Moreover, flow instability triggers prior to complete mobilization of the critical state friction angle (e.g., Yoshimine et al., 1999; Khoa et al., 2006; Daouadji et al., 2010; Andrade et al., 2013; Baki et al., 2014; Hubler et al., 2017; Lashkari, 2019; Sadrekarimi & Riveros, 2020). Sladen et al. (1985) and Lade (1992) put forward experimental evidence proclaiming that the flow instability of clean sands triggers once the effective stress path intersects the Instability Line (IL), whose slope is only a fraction of the Critical State Line (CSL) stress ratio. Afterwards, Yang (2002), Chu & Leong (2002), Mizanur & Lo (2012); Baki et al. (2014), Della et al. (2015), Lashkari et al. (2017, 2019, 2020), and Triantafyllos et al. (2020) have reported laboratory data proving non-uniqueness of IL, i.e., the flow instability stress ratio depends on void ratio and confining pressure.

Laboratory investigations in the past were frequently devoted to the flow instability of clean sands possessing uniform gradations; however, analysis of real field data has revealed that a majority of the flow instability-induced catastrophic events have occurred in sand deposits containing a notable fraction of non-plastic silt (e.g., with particle size smaller than 0.075 mm) [e.g., Lade & Yamamuro, 1997; Rahman & Sitharam, 2020]. Recent studies have indicated that non-plastic silt particles fill voids between larger sand particles and decrease the overall void ratio of the silty sands, i.e., sand-fines mixtures. However, further increasing the fraction of fines in sand changes its microstructure from "fines-in sand" to "sand-in-fines". The FC where the microstructure changes from "fines-in-sand" to "sand-in-fines" is known as the "threshold fines content", FC_{th}. Prior to reaching the FC_{th} which is commonly is in the range of 30% to 40%, most of the fine particles do not participate actively in the load-carrying microstructure. But they contribute to the decrease in overall void ratio, which does not necessarily strengthen the soil load-carrying microstructure (e.g., Thevanayagam et al., 2002; Rahman et al., 2011a, 2011b, 2014; Yang & Wei, 2012; Lashkari, 2014; Yang & Luo, 2018; Wei et al., 2020). Consequently, the critical state void ratio and constant volume shear strength of silty sands, or sand-fines mixtures, decrease with increasing fines content from FC=0 up to $FC=FC_{th}$ and thereafter, both the critical state void ratio and constant volume shear strength may improve with FC.

Ishihara & Okada (1978) first demonstrated that even a slight over-consolidation history in sands might lead to a significant increase in sand stiffness, and accordingly, lower pore-water pressure might be accumulated in Over-Consolidated (OC) specimens compared with that in Normally-Consolidated (NC) specimens of the same sand at identical relative density. Gajo & Piffer (1999) reported that an Over-Consolidation Ratio (OCR) of 3.2 might cause a 35% to 40% increase in the peak undrained shear strength of very loose sand specimens at the onset of the flow instability compared with that of NC specimens of the same density. A centrifuge modeling investigation by Adalier & Elgamal (2005) revealed that the maximum excess pore-water pressure and post-liquefaction soil settlement in OC sand specimens with $OCR\approx2$ is only 50% of those in similar NC specimens. Moreover, for the initial configurations investigated in their centrifuge testing program, a nil potential for accumulation of positive pore-water pressure and post-liquefaction settlement was observed in specimens with $OCR\approx4$. Recently, Mahmoudi et al. (2016, 2020) offered experimental evidence that sand becomes more dilative and resistant to flow liquefaction instability with an increase in OCR; however, the extent of improvement depends on the soil reconstitution method. For instance, for all OCR values within the range 1 to 8, dry funnel pluviated specimens were always more resistant than the wet tamped ones.

Thus far, flow instability of sands has been investigated primarily for clean normally consolidated (NC) sands. Whilst the existing literature highlight a noticeable impact of over-consolidation history on the constant volume (say undrained) response of granular soils, its precise impact on the slope of instability line, normalized shear strength at the onset of instability, brittleness index (I_B) and maximum excess pore-water pressure ratio is not well understood. For this reason, in this treatment, an extensive series of constant volume DSS tests covering a wide range of initial states, fines contents, and OCRs is carried out. Analysis of the laboratory data indicates that the slope of the instability line and normalized shear strength at the onset of flow instability depend on OCR and the

state parameter as defined by Been & Jefferies (1985). Moreover, it has been shown that the maximum excess pore-water pressure ratio varies with normalized shear strength and brittleness index.

2. Test soils

The coarse soil selected for the testing program is standard Firoozkuh No. 161 sand which is a commercial, factory-provided foundry sand with sub-angular particles of almost nil breakage potential under conventional stress levels, as evident in the previous pertinent studies (e.g., Farahmand et al. 2016; Lashkari et al. 2017; Lashkari et al. 2020). For Firoozkuh sand No. 161, the Particle Size Distribution (PSD) curve and Scanning Electron Microscope (SEM) photo of particles are illustrated in Fig. 1 (*see* PSD curve for FC=0), and its basic key specifications are reported in Table 1. From the results of semi-quantitative X-ray diffraction (XRD) analysis, the sand is comprised of 96.9% quartz and 3.1% calcite. The fine fraction, i.e. Firoozkuh silt, considered for preparation of silty sands, i.e. sand-fines mixtures by a systematic increase in FC is a commercial, micronized non-plastic powder derived from milling/crushing of the Firoozkuh sand particles. Hence, the mineralogical composition of the Firoozkuh sand and silt are identical. The PSD curve, as well as SEM photo of Firoozkuh silt particles, are shown in Fig. 1 (*see* PSD curve for FC=100%), and the basic properties of Firoozkuh silt are listed Table 1. It is worthwhile mentioning that both the test sand and silt were sieved on a 75 μm mesh (ASTM standard No. 200 sieve), in order to separate any fines (i.e., passing 75 μm) from the former, and sift-out any sand (i.e., retaining on 75 μm) from the latter. The silty sand mixtures were proportioned by mixing certain fractions of fines (i.e., silt) and coarse (i.e., sand) fractions in a way that the fines contents became 10%, 20%, 30%, and 40% of the total weight of mixtures. In the mixtures with higher fines contents (more than 40% of silt), the sand particles float between silt particles, and fines establish the foremost load-bearing microstructure. Such mixtures typically resemble the behavior of "fines-in-sand" rather than that of "sand-in-fines" (e.g., Thevanayagam et al., 2002; Baki et al., 2012, 2014; Rahman et al., 2011a; 2011b, 2014; Lashkari, 2014) and hence, they were excluded here from the testing program. Noticing that particles' morphology plays a central role in the mechanical behavior of granular soils (e.g., Cho et al., 2006; Yang & Wei, 2012; Wei & Yang, 2014; Jerves et al., 2016; Yang & Luo, 2018; Lashkari et al., 2020), a number of morphological measures; namely, Aspect Ratio (AR), Convexity (C), Sphericity (S), and Roundness (R) are reported in Table 1 for the Firoozkuh sand No. 161 and Firoozkuh silt.

3. Apparatus and testing methodology

The constant volume tests on NC and OC specimens were performed using an NGI-type DSS apparatus equipped with two orthogonally mounted actuators, capable of exerting vertical (normal) and shear (horizontal) forces/displacements defined/measured with respect to the specimens' cross-section. The DSS device was fully automated and enables applying both cyclic and monotonic, closed-loop strain- (displacement-) or stress- (force-) controlled loadings in vertical and shear directions. The vertical force/displacement was applied by a pneumatic jack attached to a 5 kN S-type load-cell accurate to ±0.1% of maximum load (the vertical force was precise to ±5 N). The shear force/displacement was applied via a servomotor accompanied by a 5 kN S-type load-cell with a resolution of

±0.1% of full capacity. The vertical and shear displacements were measured by LVDTs with the precision of 0.002 mm, and both were limited to 10 mm for monotonic loadings, and ±5 mm for cyclic paths. An overall view of the DSS apparatus is illustrated in Figure 2(a).

The disk shape test specimens, 70 mm in diameter and 20 mm in height, were reconstituted in four layers, each separately proportioned to the target gradation (*see* Fig. 1). The moist tamping method (Ishihara 1993; Rahman et al. 2011a) was implemented for specimen compaction, which permitted the remolding of specimens to a range of void ratios. It is important to note that during compaction of each layer (using a 66 mm diameter steel tamper), a fraction of the applied energy was transmitted to the lower layer(s). Hence, an under-compaction scheme (*see* Ladd, 1978) should be considered for the compaction of consecutive layers. Therefore, the number of tamper blows was reduced for lower layers to ensure a uniform void ratio throughout the height. The number of tamper blows for each layer is regulated by trial and error, considering the desired specimen void ratio.

As illustrated in Figs. 2(b) and 2(d), the specimens were prepared inside a rubber membrane (0.3 mm thick) surrounded by a stack of 10 low-friction Teflon-coated aluminium rings (2 mm thick and 9.5 mm wide). During the consolidation phase, the specimens were compressed to the target vertical stress of σ'_{v0} (=normal force/specimen area), during which the stiffness of the enclosing stacked rings ensures the K_0-conditions for lateral stresses. Of note, the consolidation of specimens is conducive to volume reduction, i.e., changes in void ratio, which should be counted in defining the initial void ratio (i.e., e_0) at the beginning of shear.

Throughout the shear phase, the shear displacement was exerted from the specimens' bottom and the top-platen, that bears the normal force, has no horizontal movement [see Figs. 2(c) and 2(e)]. In the case of constant volume tests wherein volume change is nil, the vertical movement of the top-platen was prohibited, and the specimen confined to stacked rings undergoes no volumetric strain. The automated closed-loop system delivered the nil movement of the top-platen of the apparatus. Therefore, when the specimen tended to dilate the vertical stress imposed on the specimen was increased, whereas the vertical stress was reduced when the specimen tended to contract. With the equipment in use, the maximum instantaneous volumetric strain of specimens was limited to ±0.01%, which corresponds to the precision LVDTs (i.e. ±0.002 mm).

4. Constant volume behavior of NC specimens

For four clean NC Firoozkuh sand specimens sheared from $\sigma'_{v0} \approx 200\,\text{kPa}$ in Figs. 3(a) and 3(b), an increase in e_0 from 0.773 (Dr=44.7%) to 0.905 (Dr=7.1%) causes the non-flow strain-hardening response in specimen with e_0=0.773 to transform gradually into flow behavior through progressive intensification of post-peak strain-softening in specimens with e_0=0.813 to 0.905. Comparison of the behaviors for the tests with e_0= 0.859 (Dr=20.2%), 0.905 (Dr=7.1%) [both with $\sigma'_{v0} \approx 200\,\text{kPa}$] and 0.876 (Dr=15.4%) [with $\sigma'_{v0} \approx 300\,\text{kPa}$] indicates that increase in σ'_{v0} amplifies post-peak softening and vulnerability to flow instability which is believed to trigger at the inception of post-peak softening under constant volume condition (e.g., Sladen et al., 1985; Lade et al., 1992; Yang, 2002; Chu & Leong, 2001; Yang & Wei, 2012; Andrade et al., 2013; Lashkari et al., 2017, 2020).

Results of four constant volume tests reported in Figs. 3(c) and 3(d) signify that increasing FC from zero to 30% motivates a gradual weakening of load-carrying microstructure and makes the NC specimens with higher FC values more susceptible to flow instability. The clean and silty specimens of Firoozkuh sand in Fig. 3 display the generic constant volume behavior of NC sands frequently reported in the literature; that is: (i) continuous strain-hardening up to the critical state for specimens in dense state, (ii) transient flow instability associated with a temporary post-peak strain-softening in medium-loose and loose states; and (iii) permanent loss of shear strength following a transient peak shear strength in loose and very loose states.

For soils sheared in DSS apparatus, stress ratio (i.e., τ/σ'_v) approaches asymptotically towards a unique critical state stress ratio (i.e., M) mathematically expressed through (e.g., Budhu, 1998; Wood et al., 1979):

$$\left(\frac{\tau}{\sigma'_v}\right)_{cs} = M = \tan\phi'_{cs} \quad (1)$$

wherein, $(\tau/\sigma'_v)_{cs}$ is stress ratio at the critical state, and ϕ'_{cs} is the critical state friction angle. Similar to Jefferies & Been (2006) and Sadrekarimi (2013), the CSL in the e vs. σ'_v plane is defined by:

$$e_{cs} = \Gamma - \lambda \ln(\sigma'_v)_{cs} \quad (2)$$

in which, e_{cs} and $(\sigma'_v)_{cs}$ are, respectively, e and σ'_v at the critical state. In Eq. (2), Γ and λ are intercept and slope of CSL in the e vs. $\ln\sigma'_v$ plane, respectively. The data for the critical (say ultimate) states of a total of 61 constant volume DSS tests on NC Firoozkuh sand specimens covering FC=0, 10%, 20%, 30%, and 40% are illustrated in Fig. 4. As seen in Fig. 4(a), the slope of CSLs in the τ vs. $\ln\sigma'_v$ plane is practically insensitive to FC. Therefore, a single CSL can reasonably be used for the specimens with FC=0 to 40%. Minimal variation of M [*see* Table 2] over a wide range of FC values from zero to 40% confirms the notion that M depends on morphologic features of particles rather than grading indices commonly expressed in terms of d_{max}, d_{50}, d_{min}, and C_u and C_c. In the e vs. σ'_v plane, a clear downward relocation of CSLs with FC is observed in Fig. 4(b). Moreover, whilst CSLs for the specimens with FC=0 to 30% are almost parallel in the e vs. σ'_v plane, cf. Fig. 4(b), further increase in FC to 40% leads to a tangible clockwise rotation of CSL [considering Table 2, $\lambda = 0.089 \pm 0.0028$ is a reasonable choice for all specimens within the range $0 \le FC \le 30\%$ which is 10% lower than $\lambda = 0.098$ for FC=40% and therefore, the FC_{th} must be in between FC=30% to 40% for the test mixtures. The concept of threshold fines content, FC_{th}, which demarcates a "fines-in-sand" from a "sand-in-fines" matrix, is an idealization of a transition zone. This transition zone may be narrow ~2% either side of a distinct FC_{th} (e.g., Rahman & Lo, 2008), or maybe "flat and wide" [for the Sydney sand–fines mixtures] (e.g., Rahman et al., 2011), about 7% either side of a not-so-distinct FC_{th}. For this reason, FC=40% data are included in this study. Of note, rotation of CSL in the e vs. σ'_v plane for fines contents greater than FC_{th} has been reported by Been et al. (1991) and Bouckovalas et al. (2003). The CSL parameters, as listed in Table 2, were obtained using multivariable regression analysis, and the corresponding CSLs were superimposed on the laboratory data as shown in Fig. 4(b).

5. Flow potential of NC specimens

The experimental data discussed in the preceding section convey that sand specimens become progressively more vulnerable to flow instability with an increase in e_0, σ'_{v0}, and FC (provided that $FC \le FC_{th}$). Similar to Sladen et al. (1985), Lade et al. (1992), Yang (2002), Chu & Leong (2002), Chu et al. (2003); Yang & Wei (2012), Andrade et al. (2013), and Lashkari et al., (2017, 2020), the inception of post-peak strain-softening in the τ vs. σ'_v plane is taken as the onset of flow instability under constant volume condition. For the NC specimens covering FC values from zero to 40%, stress ratio at the onset of flow instability [i.e., η_i $(= S_{ui}/\sigma'_{vi})$ wherein, S_{ui} and σ'_{vi} are, respectively, τ and σ'_v at the onset of flow instability] is drawn against the corresponding values of state parameter (i.e., ψ_i) in Fig. 5(a). Using the CSL parameters listed in Table 2, ψ_i in Fig. 5 is calculated through (e.g., Been & Jefferies, 2006; Sadrekarimi, 2013, 2014, 2020; Lashkari et al., 2020; Sadrekarimi & Riveros, 2020):

$$\psi_i = e - e_{cs}(\sigma'_{vi}) = e - \underbrace{\left[\Gamma - \lambda \ln \sigma'_{vi}\right]}_{e_{cs}(\sigma'_{vi})} \tag{3}$$

wherein, $e_{cs}(\sigma'_{vi})$ is e_{cs} at $\sigma'_v = \sigma'_{vi}$. Inspired by Yang (2002) and Lashkari et al. (2017, 2020), regression analysis indicates that the slope of IL in the τ vs. σ'_v (i.e., η_i) can be linked to ψ_i through:

$$\eta_i = \frac{S_{ui}}{\sigma'_{vi}} = 0.330 \exp(-3.18\psi_i) \tag{4}$$

Fig. 5(a) signifies that Eq. (4) can describe the variation of η_i with ψ_i uniquely, regardless of fines content. Data of normalized effective vertical stress at the onset of instability (i.e., $\sigma'_{vi}/\sigma'_{v0}$) depicted in Fig. 5(b) indicate that $\sigma'_{vi}/\sigma'_{v0} = 0.636$ holds reasonably for all NC specimens with FC=0 to 40%.

Normalized constant volume shear strength at the onset of flow instability (i.e., S_{ui}/σ'_{v0}) can be written in the form $S_{ui}/\sigma'_{v0} = (S_{ui}/\sigma'_{vi}) \times (\sigma'_{vi}/\sigma'_{v0})$ wherein, S_{ui}/σ'_{vi} and $\sigma'_{vi}/\sigma'_{v0}$ are, respectively, calculated through Eq. 4 [also *see* Fig. 5(a)] and Fig. 5(b). Thus, S_{ui}/σ'_{v0} becomes:

$$\frac{S_{ui}}{\sigma'_{v0}} = 0.210 \exp(-3.18\psi_i) \tag{5}$$

In Fig. 5(c), the predicted S_{ui}/σ'_{v0} vs. ψ_i curve demonstrates a reasonable correspondence with the experimental data of NC specimens for all fines contents studied here.

6. Constant volume behavior of OC specimens

The constant volume behavior of one NC (say OCR=1) and five OC clean Firoozkuh sand specimens covering OCR values from 1.5 to 6.0 (i.e., 1.5, 1.9, 3.0, 5.0 and 6.0) in the τ vs. σ'_v and τ vs. γ planes are, respectively, illustrated in parts "a" and "b" of Fig. 6. All specimens were initially subjected to $\sigma'_{vc} \approx 300\,kPa$, and consequently, five (out of six) specimens were unloaded to reach the target OCR values by reducing effective

vertical stress to $\sigma'_{v0} = \sigma'_{vc}/\mathrm{OCR}$. Despite the rather wide domain of OCRs (i.e., 1 to 6), the precise and high-quality specimen preparation procedure, taking advantage of under compaction technique together with some trial-and-error efforts, led to a relatively narrow range of e_0 values (i.e., 0.861 to 0.872) for the sand specimens prior to shear. In the clean NC specimen (say OCR=1) in Figs. 6(a) and 6(b), the flow instability triggered at $\sigma'_{vi} \approx 196.98\,\mathrm{kPa}$ and S_{ui}=49.8 kPa [γ_i (i.e., shear strain at which flow instability is triggered) =2.04%] beyond which, τ eventually dropped to ≈29.4 kPa in the post-peak softening regime of the behavior. Dissimilar to the NC specimen, τ in the specimen with OCR=1.5 mobilized without any decrease in σ'_v until $\tau \approx$22.40 kPa and thereafter, the effective stress path bent to the left. Flow instability for the clean specimen with OCR=1.5 occurred at $\sigma'_{vi} \approx 156.03\,\mathrm{kPa}$ and S_{ui}=51.55 kPa (at γ_i=1.63%). Further, the increase in OCR caused a progressive decrease in σ'_{vi}, S_{ui} and γ_i in as much as $\sigma'_{vi} \approx 54.32\,\mathrm{kPa}$, S_{ui}=20.68 kPa, and γ_i=1.64% were eventually attained for the clean specimen with OCR=6.0 in Figs. 6(a) and 6(b). The data demonstrated in parts "c" to "j" of Fig. 6 confirm similar trends for the variation of σ'_{vi}, S_{ui} and γ_i with OCR in the sand specimens containing 10, 20, 30, and 40% of non-plastic silt. For a total of 26 tests on clean and silty sand specimens whose τ vs. σ'_v and τ vs. γ responses were depicted in Fig. 6, two phenomena happen concurrently as a consequence of escalating OCR: (i) flow instability may trigger with a negligible decrease in σ'_v (*see* specimens with $4 > \mathrm{OCR} \geq 2$) or even without any noticeable decline in σ'_v (*see* specimens with $\mathrm{OCR} \geq 4$) [equally, without any tangible increase in excess pore-water pressure] and thus, $\sigma'_{vi}/\sigma'_{v0}$ increases with OCR, and (ii) on the other hand, the difference between peak (i.e., instability) and the minimum post-peak strengths decreases gradually with rising OCR leading to gradual mitigation of brittleness following the onset of flow instability.

For the mixtures with FC=0, 10%, and 30%, normalized effective stress paths in the σ'_v/σ'_{v0} vs. τ/σ'_{v0} plane, mobilization of the normalized shear strength in the τ/σ'_{v0} vs. γ plane, and accumulation of normalized excess pore-water pressure in the $\Delta u/\sigma'_{v0}$ vs. γ plane are instanced in Fig. 7. The initial parts of the normalized effective stress paths in parts "a", "d", and "g" of Fig. 7 bend to the right increasingly with elevating OCR in an approximately unique way. However, the effective stress paths begin to depart at certain dividing states and then move to the left one after another, depending on their OCRs. Afterwards, flow instability triggers once normalized effective stress paths intersect IL at the start of strain-softening. Curves for τ/σ'_{v0} vs. γ in parts "b", "e", and "h" of Fig. 7 indicate that shear strain at the onset of flow instability is almost insensitive to OCR. Finally, $\Delta u/\sigma'_{v0}$ vs. γ curves in parts "c", "f", and "i" of Fig. 7 suggest mitigation of positive $\Delta u/\sigma'_{v0}$ with increasing OCR.

7. Flow potential of OC specimens

For 39 OC specimens suffering from flow instability, data of the stress ratio at the onset of instability are drawn against the corresponding state parameter values in Fig. 8. For the

specimens with OCR=1.5 in Fig. 8(a), the distribution of the η_i vs. ψ_i data is practically identical to that for the NC specimens; however, a slight upward relocation of η_i vs. ψ_i data for the specimens with OCR≈2 is observed in Fig. 8(b). An evident increase in flow instability stress ratio is observed in parts "c" and "d" of Fig. 8 for the specimens with OCR=3.0 and OCR=4.0 to 6.2, respectively. Fig. 8 also implies that the impact (if any) of FC on flow instability stress ratio (if existent) must be minimal. Using Eq. (4) as a benchmark together with the nonlinear multivariable regression analysis, the following empirical relationship is suggested here for the increase in flow instability stress ratio with OCR:

$$\eta_i = \frac{S_{ui}}{\sigma'_{vi}} = \left\{0.40 - 0.07\exp\left[-0.233(\text{OCR}-1)^2\right]\right\}\exp(-3.18\,\psi_i) \qquad (6)$$

Of note, η_i obtained from Eq. (6) must be limited to M. Eq. (6) transforms into Eq. (4) for NC (say OCR=1) specimens as OCR gradually approaches unity. Fig. 8 demonstrates a realistic agreement between the experimental data for η_i vs. ψ_i and the corresponding predictions obtained from Eq. (6) for OCR=1, 1.5, 2.0, 3.0, and 4.0 to 6.2.

For the specimens suffering from flow instability covering FC values from zero to 40%, the experimental data depicted in Fig. 9 indicate that the normalized effective vertical stress at the onset of instability (i.e., $\sigma'_{vi}/\sigma'_{v0}$) increases steadily with OCR irrespective of FC and ψ_i (at least for the ranges of ψ_i studied here). Analysis of the laboratory data shown in Fig. 9 results in the following empirical relationship correlating $\sigma'_{vi}/\sigma'_{v0}$ with OCR:

$$\frac{\sigma'_{vi}}{\sigma'_{v0}} = 0.636 + 0.528\left(\frac{\text{OCR}-1}{\text{OCR}}\right) \qquad (7)$$

The $\sigma'_{vi}/\sigma'_{v0}$ lines predicted from Eq. (7) for OCR=1, 1.5, 2, 3, and 6 are superimposed on the experimental data in Fig. 9.

Using Eqs. (6) and (7) along with ordinary algebra operations [*see* the proof for Eq. (5)] yields the following empirical equation for Normalized Instability Shear Strength (NISS) for both the OC and NC specimens:

$$\frac{S_{ui}}{\sigma'_{v0}} = \left(1.164 - \frac{0.528}{\text{OCR}}\right)\left\{0.40 - 0.07\exp\left[-0.233(\text{OCR}-1)^2\right]\right\}\exp(-3.18\,\psi_i) \qquad (8)$$

For the range $1 \le \text{OCR} \le 6.2$ studied here, the term $\left(1.164 - \frac{0.528}{\text{OCR}}\right)\left\{0.40 - 0.07\exp\left[-0.233(\text{OCR}-1)^2\right]\right\}$ in Eq. (8) can be estimated accurately by $0.445 - 0.235\exp\left[-0.57(\text{OCR}-1)\right]$ (with r^2=0.999) and accordingly, Eq. (8) may be simplified into:

$$\frac{S_{ui}}{\sigma'_{v0}} = \left\{0.445 - 0.235\exp\left[-0.57(\text{OCR}-1)\right]\right\}\exp(-3.18\,\psi_i) \qquad (9)$$

For the specimens with OCR=1.5, 2.0, 3.0, and 4.0 to 6.0, the predicted curves for (S_{ui}/σ'_{v0}) vs. ψ_i are superimposed on the laboratory data in parts "a" to "d" of Fig. 10.

8. Brittleness index

For sand specimens suffering from limited or complete flow instability, Brittleness index (i.e., I_B) is defined through (e.g., Bishop, 1971; Jefferies & Been, 2006; Lashkari et al., 2019):

$$I_B[\%] = 100\left(1 - \frac{\tau_{min}}{\tau_{max}}\right) \tag{10}$$

wherein, τ_{max} is the maximum shear strength attained at the onset of transient/permanent flow instability (i.e., S_{ui}), and τ_{min} is the minimum post-instability shear strength. τ_{min} is the momentary minimum shear strength in medium-loose sands exhibiting quasi steady-state response or the critical state shear strength in loose and very loose sands suffering from permanent loss of shear strength. I_B varies between zero for the specimens with non-flow response and unity for the specimens losing their shear strength completely in the post-instability regime of the behavior.

In Figs. 3(a) and 3(b), I_B=0 holds for the specimen with e_0=0.773 ($\sigma'_{v0} \approx 200$ kPa) because it demonstrates continuous strain-hardening in the entire shear strain domain studied here. For the specimen with e_0=0.813, sand stiffness (i.e., the slope of the τ vs. γ curve) declines significantly beyond $\gamma \approx 1.97$ %. This specimen demonstrates a very mild limited flow instability for which I_B=3% is calculated. Further increase in e_0 escalates brittleness index dramatically in a way that I_B≈16% and I_B≈62% are, respectively, obtained for the specimens with e_0=0.859 (Dr=20.2%) and 0.905 (Dr=7.1%). An increase in σ'_{v0} from 200 kPa to 300 kPa leads to I_B≈57% in the specimen with e_0=0.876 (Dr=15.4%). The laboratory data reported in Figs. 3(c) and 3(d) highlight gradual degradation of strain-hardening with increasing FC to the extent that I_B=0 for the specimens with FC=0% and 10% while this rises progressively to I_B=20% and I_B=31% for the specimens with FC=20% and FC=30%, respectively. The latter discussions of the laboratory data clearly indicate that I_B levels up with increase in e_0, σ'_{v0}, and $FC\,(\leq FC_{th})$.

For a total of 67 specimens with FC=0 to 40% experiencing flow instability, data for I_B vs. (S_{ui}/σ'_{v0}) are illustrated in Fig. 11 wherein, trends for the variation of I_B with S_{ui}/σ'_{v0} for OCR=1.0, 1.5, 2.0, 3.0 and 5.2 to 6.0 are almost parallel irrespective of initial state and FC. Analysis of the experimental data has revealed that a unique trend for all OCRs exists in the I_B vs. $S_{ui}/[(1+0.79\ln OCR)\sigma'_{v0}]$ plane. Taking into consideration of the aforementioned simplifying point in the multivariable regression analysis, the following empirical relationship is suggested here to represent the variation of I_B with (S_{ui}/σ'_{v0}) and OCR irrespective of FC:

$$I_B = 0.50\left\{1 - \tanh\left[\frac{21.6}{1+0.79\ln OCR}\cdot\left(\frac{S_{ui}}{\sigma'_{v0}}\right) - 3.13\right]\right\} \tag{11}$$

Using Eq. (11), the predicted curves for the variation of I_B with I_B vs. (S_{ui}/σ'_{v0}) for the specimens with OCR=1.0, 1.5, 2.0, 3.0 and 5.2 to 6.0 are depicted against the corresponding data in Fig. 11.

9. Maximum pore-water pressure ratio

The maximum excess pore-water pressure ratio [of note, the excess pore-water pressure ratio is calculated through $r_u = \frac{\Delta u}{\sigma'_{v0}} = \frac{\sigma'_{v0} - \sigma'_v}{\sigma'_{v0}} = 1 - \frac{\sigma'_v}{\sigma'_{v0}}$] in the constant volume DSS tests is calculated through:

$$(r_u)_{max} = 1 - \frac{(\sigma'_v)_{min}}{\sigma'_{v0}} \quad (12)$$

For medium-loose specimens exhibiting limited flow instability, $(\sigma'_v)_{min}$ is the minimum vertical effective stress which was achieved at the quasi steady-state/phase transformation (e.g., Yoshimine et al., 1998). However, for very loose sand specimens suffering from permanent flow instability, $(\sigma'_v)_{min}$ is the minimum vertical effective stress at large shear strains in the post-instability regime of the behavior. Through some ordinary algebra, Eq. (12) can be rearranged in the form:

$$(r_u)_{max} = 1 - \frac{\left(\frac{\tau_{min}}{S_{ui}}\right) \cdot \left(\frac{S_{ui}}{\sigma'_{v0}}\right)}{\left(\frac{\tau_{min}}{(\sigma'_v)_{min}}\right)} \quad (13)$$

Recalling definition of I_B [*see* Eq. (10)], the term $\left(\frac{\tau_{min}}{S_{ui}}\right)$ in the nominator of Eq. (13) equals $(1 - I_B)$. In addition, the term $\left(\frac{S_{ui}}{\sigma'_{v0}}\right)$ in the nominator of Eq. (13) can be calculated through either Eq. (8), or (9). Dense and medium-dense sand specimens are inherently resistant to flow instability (e.g., Been & Jefferies, 1985; Yoshimine et al., 1998; Rahman et al., 2011a). For the medium-loose to very loose NC specimens of Firoozkuh clean and silty sand specimens covering FC=0% to 40%, the data for $\frac{\tau_{min}}{(\sigma'_v)_{min}}$ [*see* the denominator of Eq. (13)] in Fig. 12 only vary in a narrow range with an average of 0.479 [-]. This implies that the average $\frac{\tau_{min}}{(\sigma'_v)_{min}}$ in medium-loose to very loose NC Firoozkuh sand specimens is roughly 92% of the mean slope of CSL in the τ vs. σ'_v plane.

Now, substitution of $\left(\frac{\tau_{min}}{S_{ui}}\right) = 1 - I_B$ and $\frac{\tau_{min}}{(\sigma'_v)_{min}} \approx 0.479$ in Eq. (13) yields:

$$(r_u)_{max} = 1 - 2.09\,(1 - I_B) \cdot \left(\frac{S_{ui}}{\sigma'_{v0}}\right) \quad (14)$$

Recalling that I_B itself is a function of S_{ui}/σ'_{v0} and OCR [*see* Eq. (11)], Eq. (14) can be applied to predict the maximum excess pore-water pressure ratio of normally- and over-consolidated specimens. For OCR=1.0, 1.5, 2.0, 3.0, and 5.0 to 6.2, the predicted curves for the variation of $(r_u)_{max}$ with S_{ui}/σ'_{v0} are drawn together with the laboratory data in

Fig. 13 wherein, continuous decrease in $(r_u)_{max}$ with increasing S_{ui}/σ'_{v0} as well as an increase in $(r_u)_{max}$ with OCR are accurately captured by Eq. (14).

10. Conclusions

Loose and very loose sands are prone to flow instability under constant volume shear. An experimental investigation carried out in the past have indicated that Normally Consolidated (NC) sands in the loose state may become unstable prior to complete mobilization of the critical state friction angle once their effective stress path intersect Instability Line (IL). Although it is well known that over-consolidation may affect sand behavior profoundly, its impacts on the mechanical behavior of OC sands suffering from flow instability are not fully understood. As an attempt to fill this gap, an extensive experimental investigation on flow instability of OC and NC sands were reported here. The experimental program covered a wide range of initial states, fines contents, and over-consolidations ratios. The inferences drawn from this study are:

- Both OC and NC sands in the loose and very loose states are susceptible to flow instability.
- At identical normalized effective vertical stress (i.e., σ'_v/σ'_{v0}), over-consolidation stretches effective stress paths to the left and magnifies normalized shear strength (i.e., τ/σ'_{v0}) at the onset of flow instability.
- Shear strain at the onset of flow instability is almost insensitive to OCR.
- Over-consolidation in loose and very loose sands may lead to a lower accumulation of positive excess-pore water pressure prior to the onset of flow instability.
- At an identical value of state parameter (ψ_i), the slope of instability line, normalized vertical effective stress at the onset of instability (i.e., $\sigma'_{vi}/\sigma'_{v0}$), and normalized shear strength at the onset of flow instability (i.e., S_{ui}/σ'_{v0}) increase with OCR.
- At the same S_{ui}/σ'_{v0}, an increase in OCR leads to an increase in brittleness index and maximum pore-water pressure ratio.

References

Adalier K, Elgamal A (2005). Liquefaction of over-consolidated sand: a centrifuge investigation. Journal of Earthquake Engineering, 9 (special issue 1): 127-150.

Andrade JE. Ramos AM, Lizcano A (2013). Criterion for flow liquefaction instability. Acta Geotechnica, 8: 525-535.

Baki MAL, Rahman MM, Lo SR (2014). Predicting onset of cyclic instability of loose sand with fines using instability curves. Soil Dynamics and Earthquake Engineering, 61-62: 140-151.

Baki MAL, Rahman MdM, Lo SR, Gnanendran CT (2012). Linkage between static and cyclic liquefaction of loose sand with a range of fines contents. Canadian Geotechnical Journal, 49(8): 891-906.

Been K, Jefferies MG (1985). A state parameter for sands. Géotechnique, 35(2): 99-112.

Been K, Jefferies MG, Hachey J (1991). The critical state of sands. Géotechnique, 41(3): 365-381.

Bishop AW (1971). Shear strength parameters for undisturbed and disturbed soil specimens. in: Parry RHG (ed.) Proceedings on Roscoe Memorial Symposium. Cambridge University Press, Cambridge: 3-58.

Bouckovalas GD, Andrianopoulos KI, AG Papadimitriou (2003). A critical state interpretation for the cyclic liquefaction resistance of silty sands. Soil Dynamics and Earthquake Engineering, 23(2): 115-125.

Budhu M (1988). Failure state of a sand in simple shear. Canadian Geotechnical Journal, 23: 395-400.

Cho G, Dodds J, Santamarina JC (2006). Particle shape effects on packing density, stiffness and strength: natural and crushed sands. Journal of Geotechnical and Geoenvironmental Engineering, 132(5): 591-602.

Chu J, Leong WK (2001). Pre-failure strain softening and pre-failure instability of sand: a comparative study. Géotechnique, 51(4): 311-321.

Chu J, Leong WK (2002). Effect of fines on instability behavior of loose sand. Géotechnique, 52(10): 751-755.

Chu J, Leroueil S, Leong WK (2003). Unstable behavior of sand and its implication for slope stability. Canadian Geotechnical Journal, 40(5): 873-885.

Daouadji A, AlGali H, Darve F, Zeghloul A (2010). Instability of granular materials: experimental evidence of diffuse mode of failure for loose sands. Journal of Engineering Mechanics, 136(5): 575-588.

Della N, Belkhatir M, Arab A, Canou J, Dupla J-C (2015). Undrained monotonic response and instability of medium dense sandy soil. Marine Georesources and Geotechnology, 33(6): 487-495.

Farahmand K, Lashkari A, Ghalandarzadeh A (2016). Firoozkuh sand: introduction of a benchmark for geomechanical studies. Iranian Journal of Science and Technology, Transaction of Civil Engineering, 40(2): 133-148.

Gajo A, Piffer L (1999). The effects of preloading history on the undrained behavior of saturated loose sand. Soils and Foundations, 39(6): 43-54.

Hubler JF, Athanasopoulos-Zekkos A, Zekkos D (2017). Monotonic, cyclic, and postcyclic simple shear response of three uniform gravels in constant volume condition. J Geotech Geoenviron Eng, 143(9), DOI: 10.1061/(ASCE)GT.1943-5606.0001723

Ishihara K (1993). Liquefaction and flow failure during earthquake, Géotechnique, 43(3): 351-414.

Ishihara K, Okada S (1978). Yielding of overconsolidated sand and liquefaction model under cyclic stress. Soils and Foundations, 18(1): 57-72.

Jefferies M, Been K (2015). Soil liquefaction: a critical state approach. CRC Press, Taylor & Francis Group, Boca Raton, FL 33487-2742, USA.

Jerves AX, Kawamoto RY, Andrade JE (2016). Effect of grain morphology on critical state: a computational analysis. Acta Geotechnica, 11(3): 493-503.

Khoa HDV, Georgopoulos IO, Darve F, Laouafa F (2006). Diffuse failure in geomaterials: experiments and modeling. Computers and Geotechnics, 33: 1-14.

Ladd R (1978). Preparing test specimens using undercompaction. Geotechnical Testing Journal, 1(1): 16-23.

Lade PV (1992). Static instability and liquefaction of loose fine sandy slopes. Journal of Geotechnical Engineering, 118(1): 51-71.

Lade PV, Yamamuro JA (2011). Evaluation of static liquefaction of silty sand slopes. Canadian Geotechnical Journal, 48(2): 247-264.
Lashkari A (2014). Recommendations for extension and re-calibration of an existing sand constitutive model taking into account varying non-plastic fines content. Soil Dynamics and Earthquake Engineering, 61-62: 212-238.
Lashkari A, Karimi A, Fakharian K, Kaviani-Hamamedani F (2017). Prediction of undrained behavior of isotropically and anisotropically consolidated Firoozkuh sand: instability and flow liquefaction. Int J Geomech, 17(10), 04017083: 1-17.
Lashkari A, Khodadadi M, Binesh SM, Rahman MdM (2019). Instability of particulate assemblies under constant shear drained stress path: DEM approach. Int J Geomech, 19(6), 04019049: 1-21.
Lashkari A, Yaghtin MS (2018). Sand flow liquefaction instability under shear-volume coupled strain paths. Géotechnique, 68(11): 1002-1024.
Lashkari A, Falsafizadeh SR, Shourijeh PT, Alipour MJ (2020). Instability of loose sand in constant volume direct simple shear tests in relation to particle shape. Acta Geotechnica, 15: 2507-2527.
Mahmoudi Y, Cherif Taiba A, Belkhatir M, Schanz T (2016). Experimental investigation on undrained shear behavior of overconsolidated sand-silt mixtures: effect of sample reconstitution. Geotechnical Testing Journal, 39(3): 515-523.
Mahmoudi Y, Cherif Taiba A, Hazout L, Belkhatir M, Baille W (2020). Packing density and overconsolidation ratio effects on the mechanical response of granular soils. Geotech Geol Eng, 38: 723-742.
Mizanur RM, Lo SR (2012). Predicting the onset of static liquefaction of loose sand with fines. ASCE Journalof Geotechnical and Geoenvironmental Engineering, 138(8): 1037-1041.
Monkul MM, Gültekin C, Gülver M, Akın Ö, Eseller-Bayat E (2015). Estimation of liquefaction potential from dry and saturated sandy soils under drained constant volume cyclic simple shear loading. Soil Dynamics and Earthquake Engineering, 75: 27-36.
Rahman MdM, Lo SR, Gnanendran CT (2011). On equivalent granular void ratio and steady state behavior of loose sand with fines. Canadian Geotechnical Journal, 45(10): 1439-1456.
Rahman MdM, Lo SR, Baki MdAL (2011). Equivalent granular state parameter and undrained behavior of sandfines mixtures. Acta Geotechnica, 6: 183-194.
Rahman MM, Baki MAL, Lo SR (2014). Prediction of undrained monotonic and cyclic liquefaction behavior of sand with fines based on the equivalent granular state parameter. International Journal of Geomechanics, 14(2): 254-266.
Rahman MM, Sitharam TG (2020). Cyclic liquefaction screening of sand with non-plastic fines: critical state approach. Geosccience Frontiers, 11(2): 429-438.
Sadrekarimi A (2013). Influence of state and compressibility of liquefied strength of sands. Canadian Geotechnical Journal, 50(10): 1067-1076.
Sadrekarimi A (2014). Effect of mode of shear on static liquefaction analysis. Journal of Geotechnical and Geoenvironmental Engineering, 140(2), 04014069:1-12, DOI:10.1061/(ASCE)GT.1943-5606.0001182.
Sadrekarimi A (2020). Forewarning of static liquefaction landslides. Journal of Geotechnical and Geoenvironmental Engineering, 146(9): 04020090.

Sadrekarimi A, Riveros GA (2020). Static liquefaction analysis of the Fundão Dam failure. Geotechnical and Geological Engineering, in press.
Sladen JA, D'Hollander RD, Krahn J (1985). The liquefaction of sands, a collapse surface approach. Canadian Geotechnical Journal, 22: 564-578.
Song S, Sun Y (2019). Flow liquefaction instability and the permissible range of fractional order of sand. European Journal of Environmental and Civil Engineering, DOI: 10.1080/19648189.2019.1703122.
Thevanayagam S, Shenthan T, Mohan S, Liang J (2002). Undrained fragility of clean sands, silty sands, and sandy silts. Journal of Geotechnical and Geoenvironmental Engineering, 128(10): 849-859.
Triantafyllos PK, Georgiannou VN, Dafalias YF, Georgopoulos I-O (2020). New findings on the evolution of instability surface of loose sand. Acta Geotechnica, DOI: 10.1007/s11440-019-00887-7
Wanatowski D, Chu J (2012). Factors affecting pre-failure instability of sand under plane-strain condition. Géotechnique, 62(2): 121-135.
Wijewickreme D, Soysa A (2016). A stress-strain pattern based criterion to assess cyclic shear resistance of soil from laboratory element tests. Canadian Geotechnical Journal, 53(9): 1460-1473.
Wei LM, Yang J (2014). On the role of grain shape in static liquefaction of sand-fine mixtures . Géotechnique, 64(9): 740-745.
Wei X, Yang J, Zhou Y-G, Chen Y (2020). Influence of particle-size disparity on cyclic liquefaction resistance of silty sands. Géotechnique Letters, 10: 1-7.
Wood DM, Drescher A, Budhu M (1979). On the determination of the stress state in the simple shear apparatus. Geotechnical Testing Journal, 2(4): 211-221.
Wu QX, Xu TT, Yang ZX (2019). Diffuse instability of granular material under various drainage conditions: discrete element simulation and constitutive modeling. Acta Geotechnica. DOI: 10.1007/s11440-019-00885-9
Yang J, Luo XD (2018). The critical state friction angle of granular materials: does it depend on grading? Acta Geotechnica, 13(3): 535-547.
Yang J, Wei LM (2012). Collapse of loose sand with the addition of fines: the role of particle shape. Géotechnique, 62(12): 1111-1125.
Yang J (2002). Non-uniqueness of flow liquefaction line for loose sand. Géotechnique, 52(10): 757-760.
Yoshimine M, Ishihara K, Vargas W (1998). Effects of principal stress direction and intermediate principal stress on undrained shear behavior of sand. Soils and Foundations, 38(3): 179-188.
Yoshimine M, Robertson PK, (Fear) Wride CE (1999). Undrained shear strength of clean sands to trigger flow liquefaction. Can Geotech J, 36: 891-906.
Zhang W, Askarinejad A (2019). Centrifuge modeling of submarine landslides due to static liquefaction. Landslides, 16: 1921-1938.

Table 1. Physical properties of Firoozkuh sand No. 161 and Firoozkuh silt used in this study

Material	G_s [-]	d_{50} [mm]	C_u [-]	C_c [-]	e_{max} [-]	e_{min} [-]	AR § [-]	C ¶ [-]	S † [-]	R ‡ [-]
sand	2.65	0.270	1.38	1.03	0.930	0.579	0.723	0.940	0.899	0.580
silt	2.65	0.038	5.44	2.18	1.461	0.664	0.714	0.909	0.767	0.555

§: mean aspect ratio of particles
¶: mean convexity of particles
†: mean sphericity of particles
‡: mean roundness of particles

Table 2. Critical state parameters for NC Firoozkuh sand specimens with varying fines contents

Soil	Γ [-]	λ [-]	M [-]	ϕ'_{cs} [deg.]
Clean Firoozkuh sand (FC = 0 %)	1.233	0.087	0.526	27.74
Firoozkuh silty sand (FC = 10 %)	1.194	0.093	0.526	27.74
Firoozkuh silty sand (FC = 20 %)	1.107	0.087	0.530	27.92
Firoozkuh silty sand (FC = 30 %)	1.105	0.089	0.513	27.16
Firoozkuh silty sand (FC = 40 %)	1.132	0.098	0.528	27.83

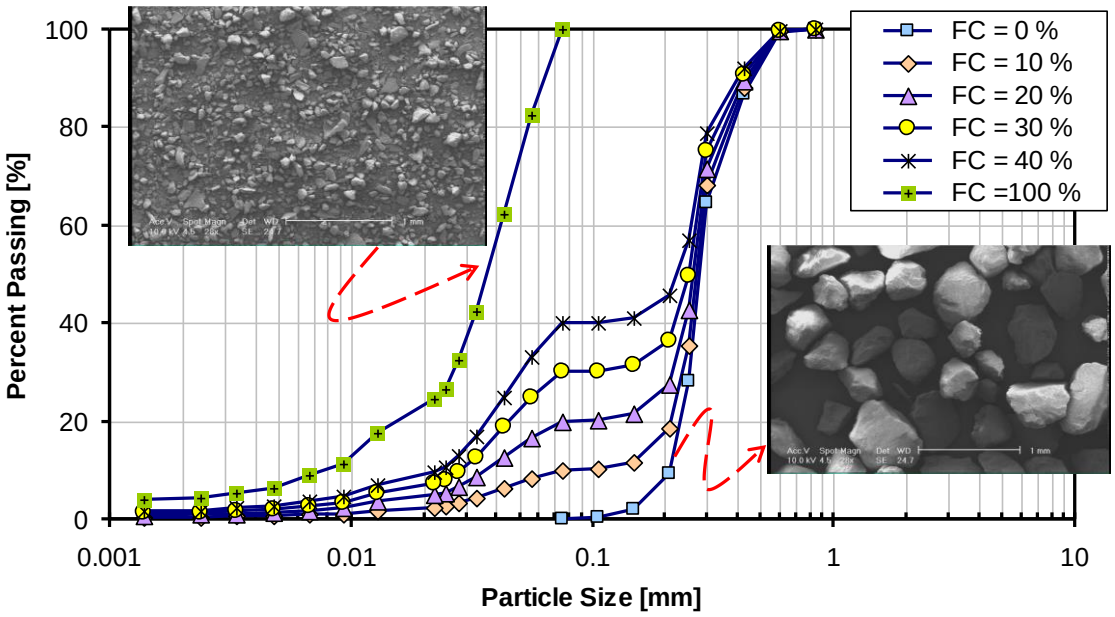


Fig. 1. Particle size distribution curves for clean host Firoozkuh sand No. 161 (*see* PSD curve for FC= 0% and the SEM photo in the right bottom for overall morphology of the sand particles), Firoozkuh silt (*see* PSD curve for FC= 100% and the SEM photo in the left above for overall morphology of the silt particles), and mixtures of Firoozkuh sand and Firoozkuh silt with 10%, 20%, 30%, and 40% fines content

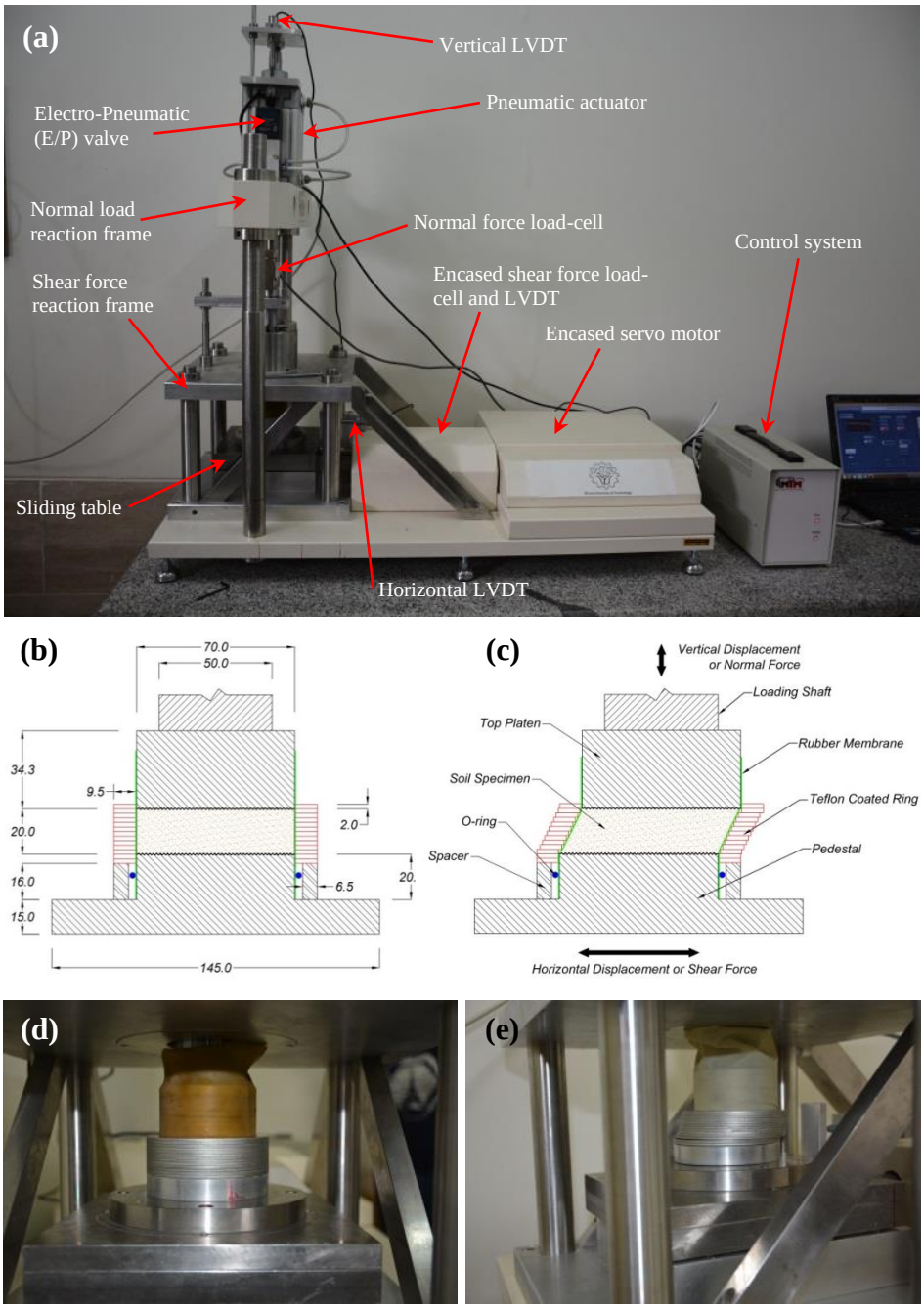


Figure 2. Views of NGI-type DSS apparatus: (a) general layout of apparatus and testing system, (b) dimensions and components of the DSS cell, (c) schematic view of the DSS cell elements, (d) specimen undergoing consolidation (prior to shear), and (e) the final stage of a deformed specimen sheared under constant volume condition

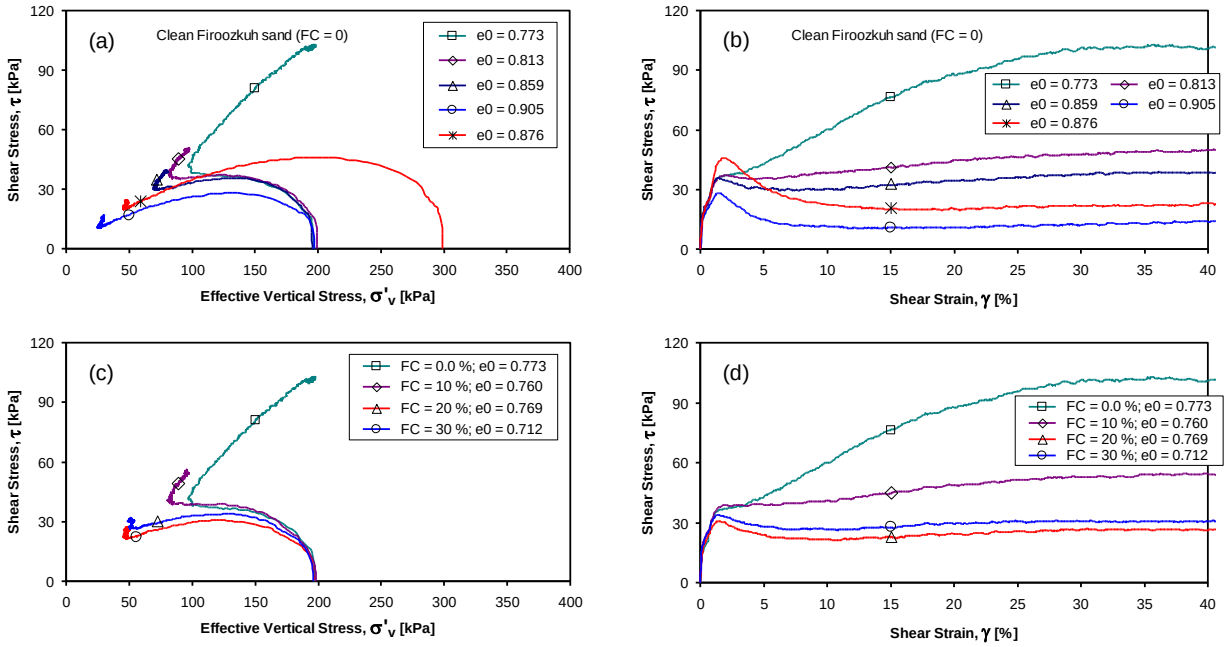


Fig. 3. General constant volume behavior of clean and silty specimens of NC Firoozkih sand in the τ vs. σ'_v and τ vs. γ planes: (a) and (b) influence of initial void ratio and vertical effective stress on the constant volume responses of five clean specimens; (c) and (d) influence of fines content on constant volume responses

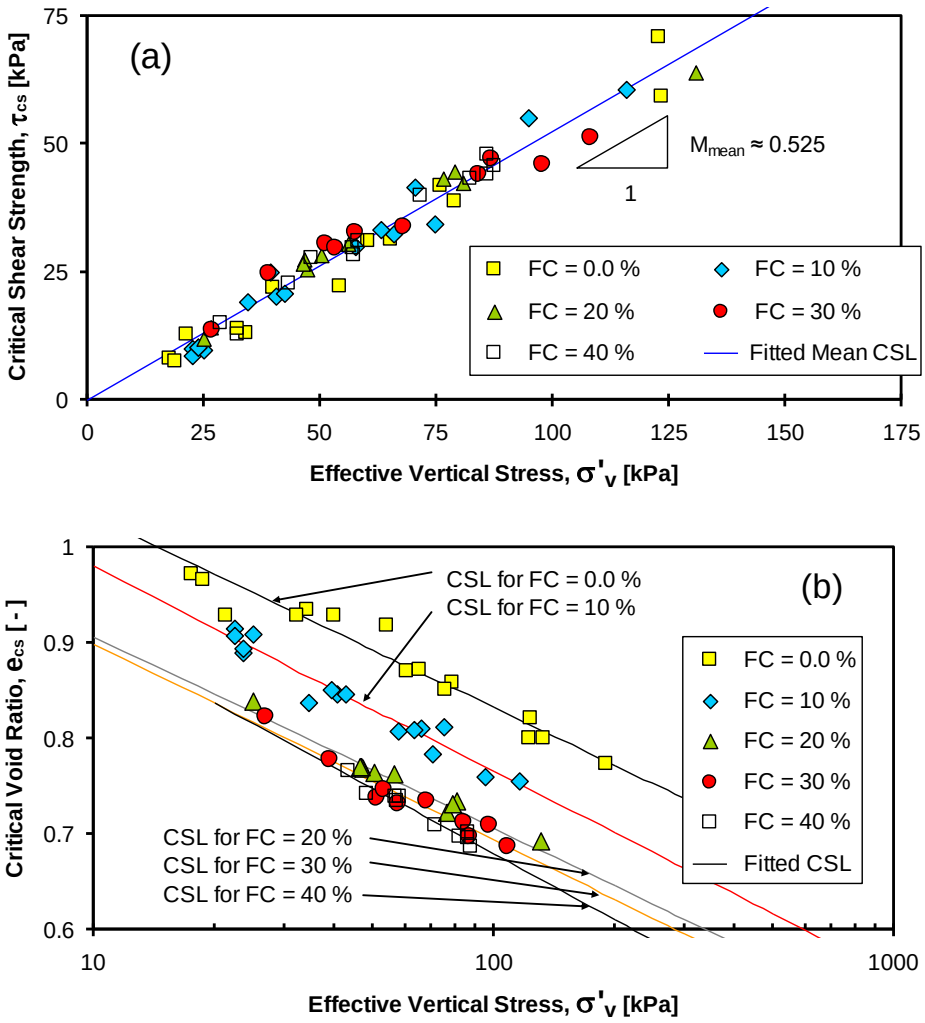


Fig. 4. CSLs for NC Firoozkuh sand specimens with varying fines contents in: (a) τ vs. σ'_v; and (b) e vs. σ'_v planes

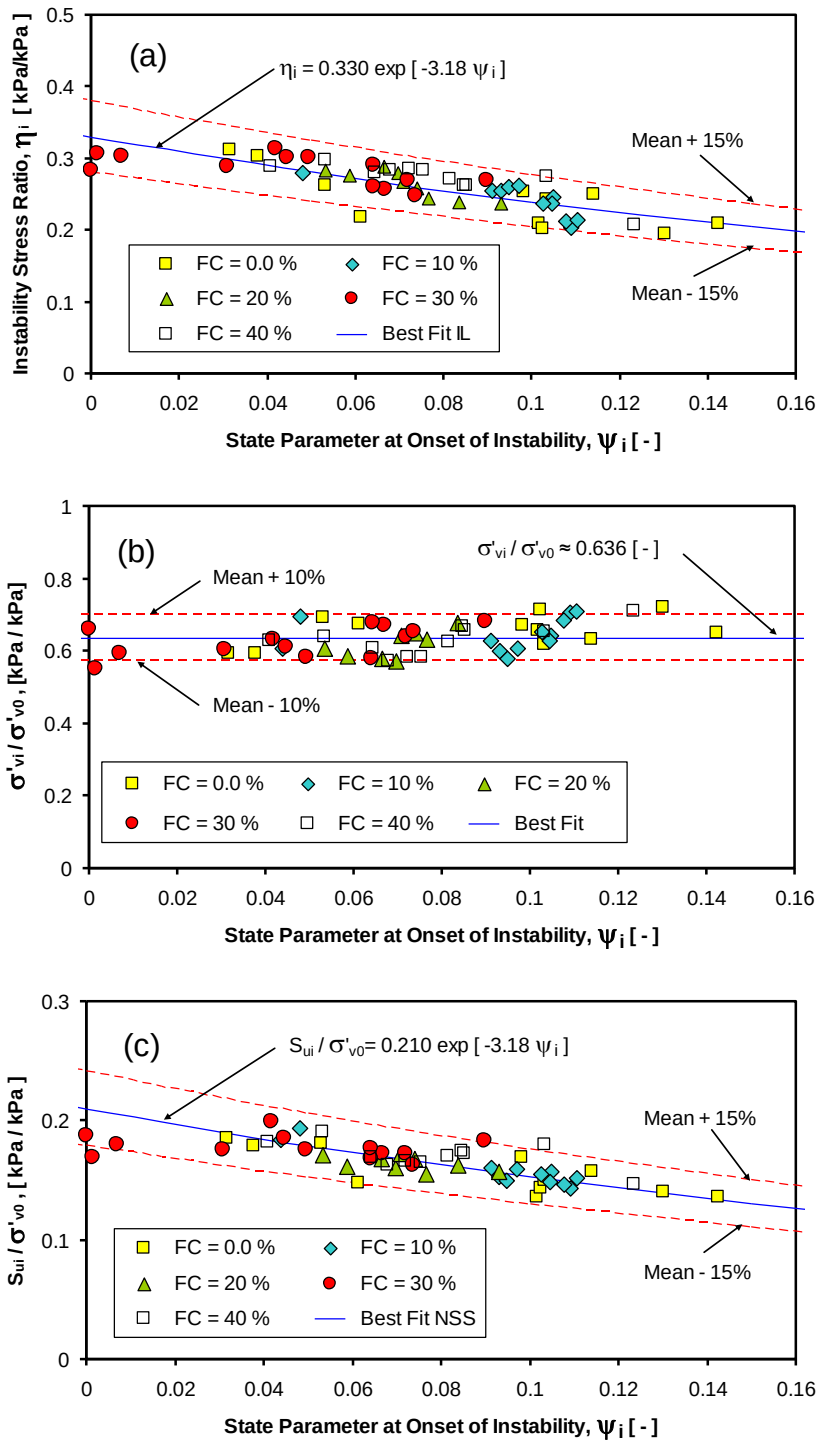


Fig. 5. Variations of: (a) instability stress ratio, (b) normalized vertical effective stress, and (c) normalized constant volume shear strength, at the onset of flow instability in NC Firoozkuh sand specimens

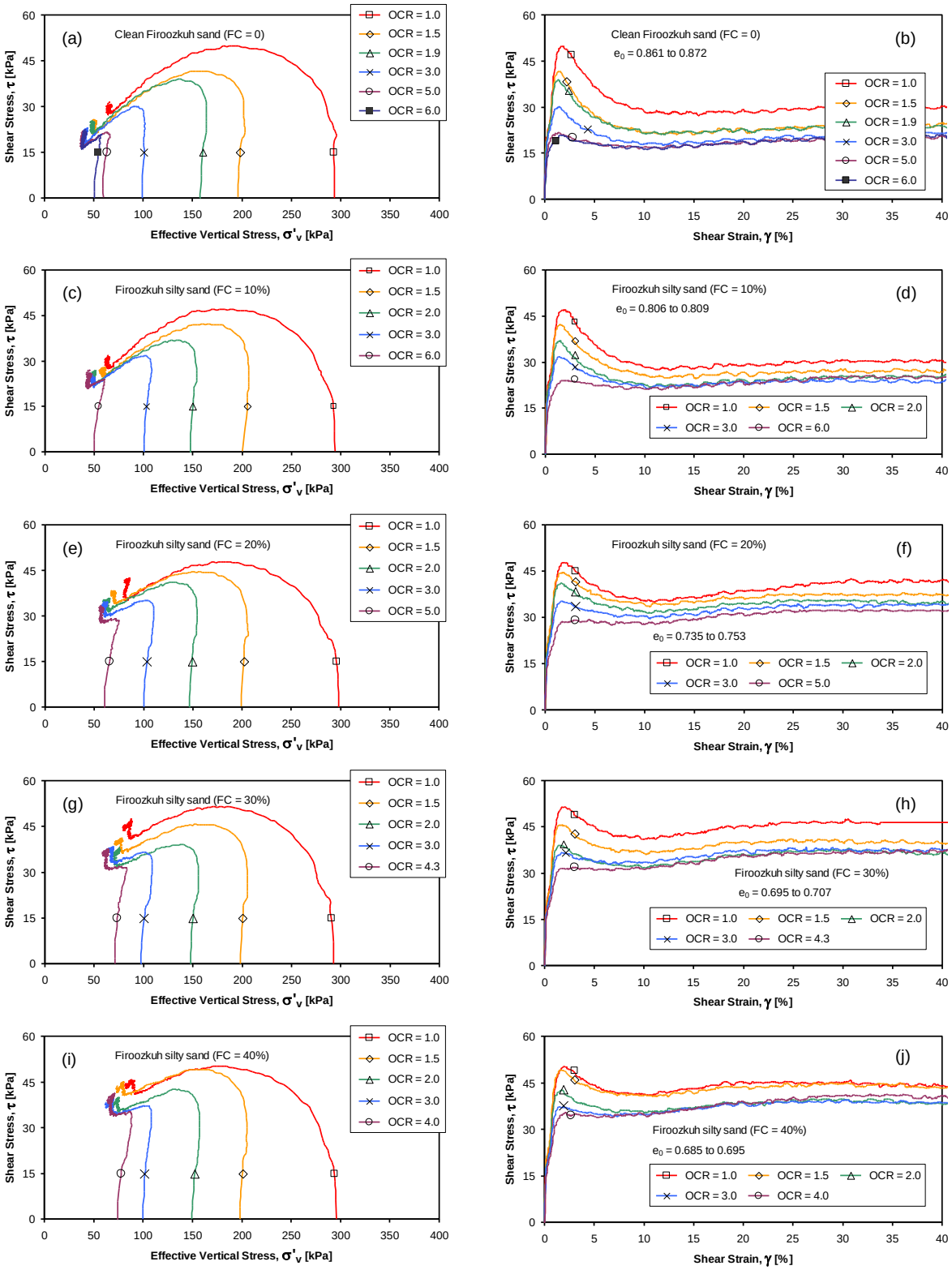


Fig. 6. Constant volume behavior of clean and silty specimens of OC Firoozkuh sand in the τ vs. σ'_v and τ vs. γ planes: (a) and (b) FC=0.0%; (c) and (d) FC=10%; (e) and (f) FC=20%; (g) and (h) FC=30%; (i) and (j) FC=40%

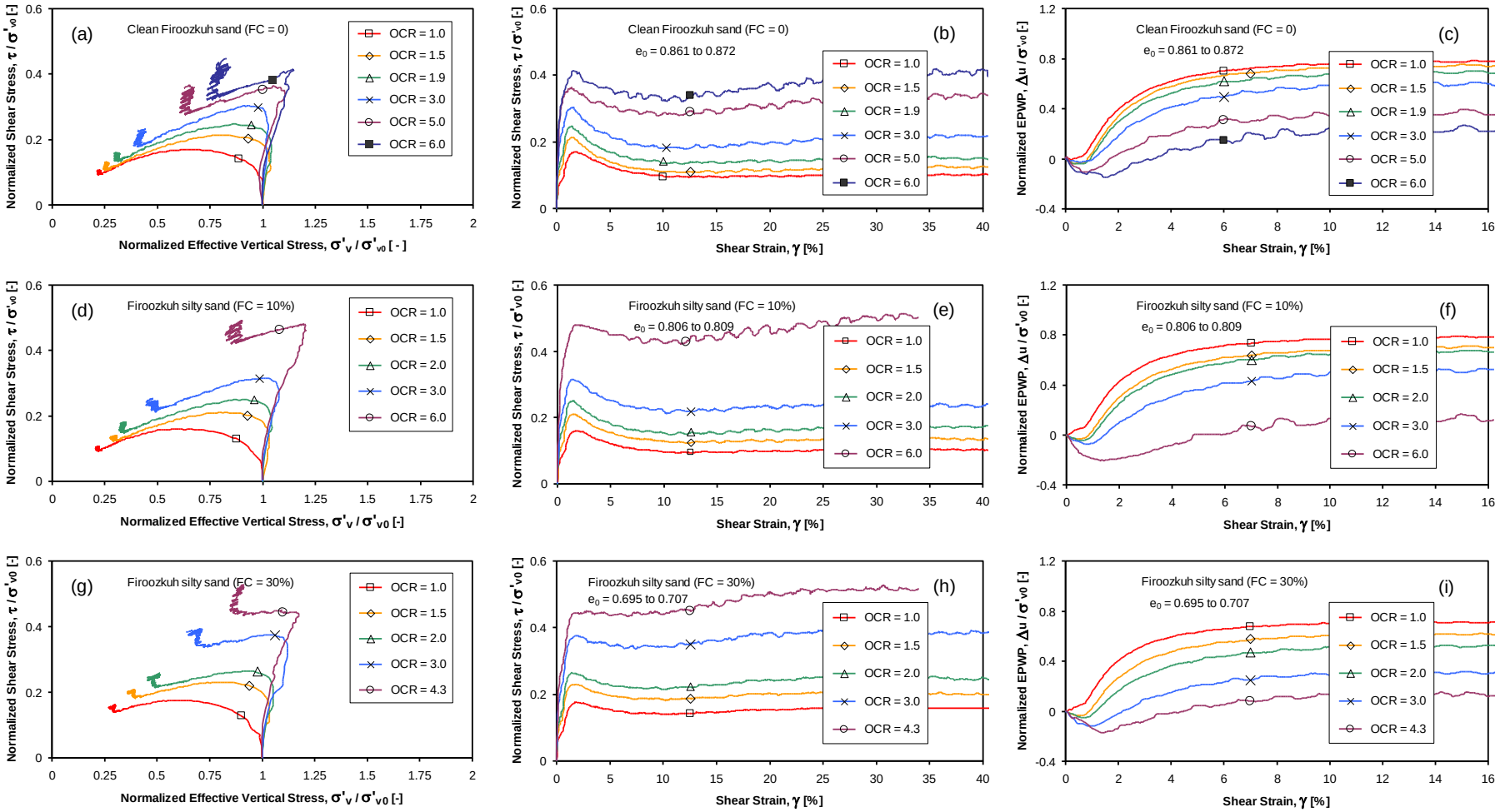


Fig. 7. Normalized constant volume behavior of clean and silty specimens of OC Firoozkuh sand in the τ/σ'_{v0} vs. σ'_v/σ'_{v0}, τ/σ'_{v0} vs. γ and $\Delta u/\sigma'_{v0}$ vs. γ planes: (a) and (b) FC=0.0%; (c) and (d) FC=10%; (e) and (f) FC=30%

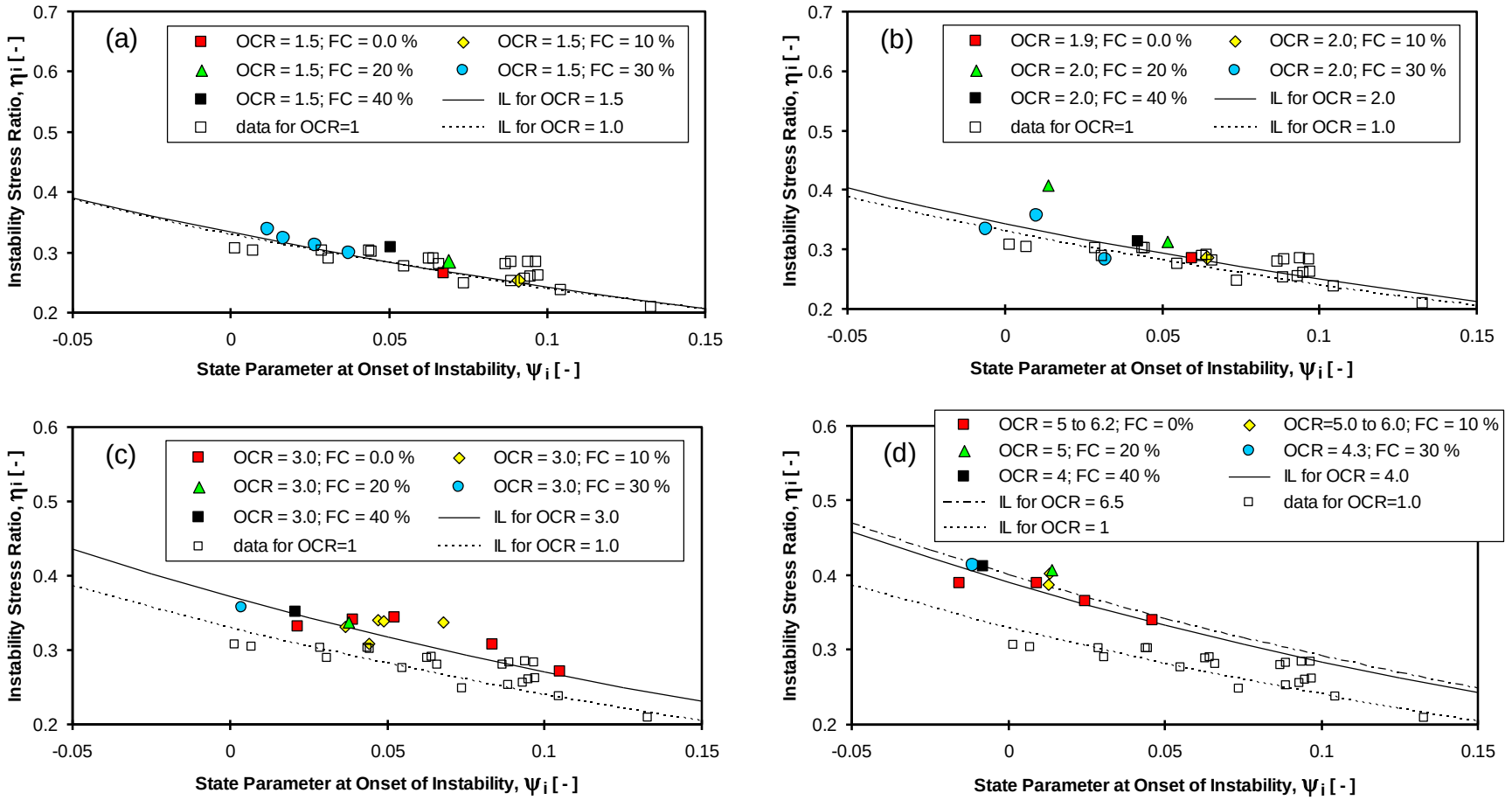


Fig. 8. Variation of instability stress ratio in over-consolidated Firoozkuh sand specimens for: (a) OCR=1.5, (b) OCR=2.0, (c) OCR=3.0, (d) OCR=4.0 to 6.2

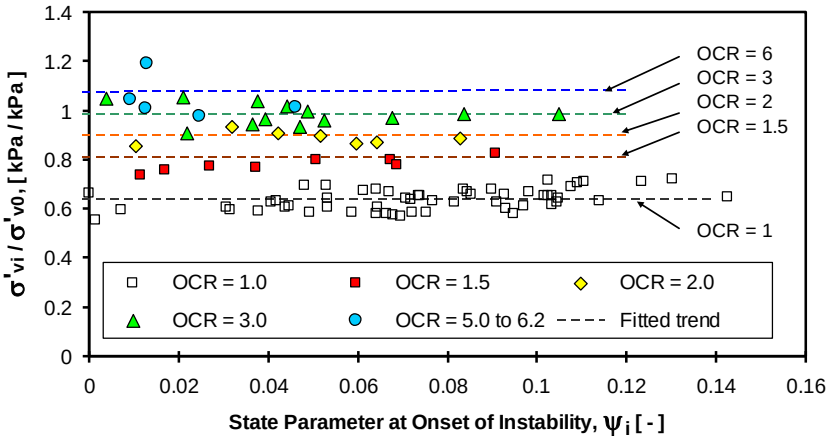


Fig. 9. Variation of $\frac{\sigma'_{vi}}{\sigma'_{v0}}$ with ψ_i at the onset of flow instability in normally- and over-consolidated Firoozkuh sand specimens with FC=0, 10%, 20%, 30%, and 40%

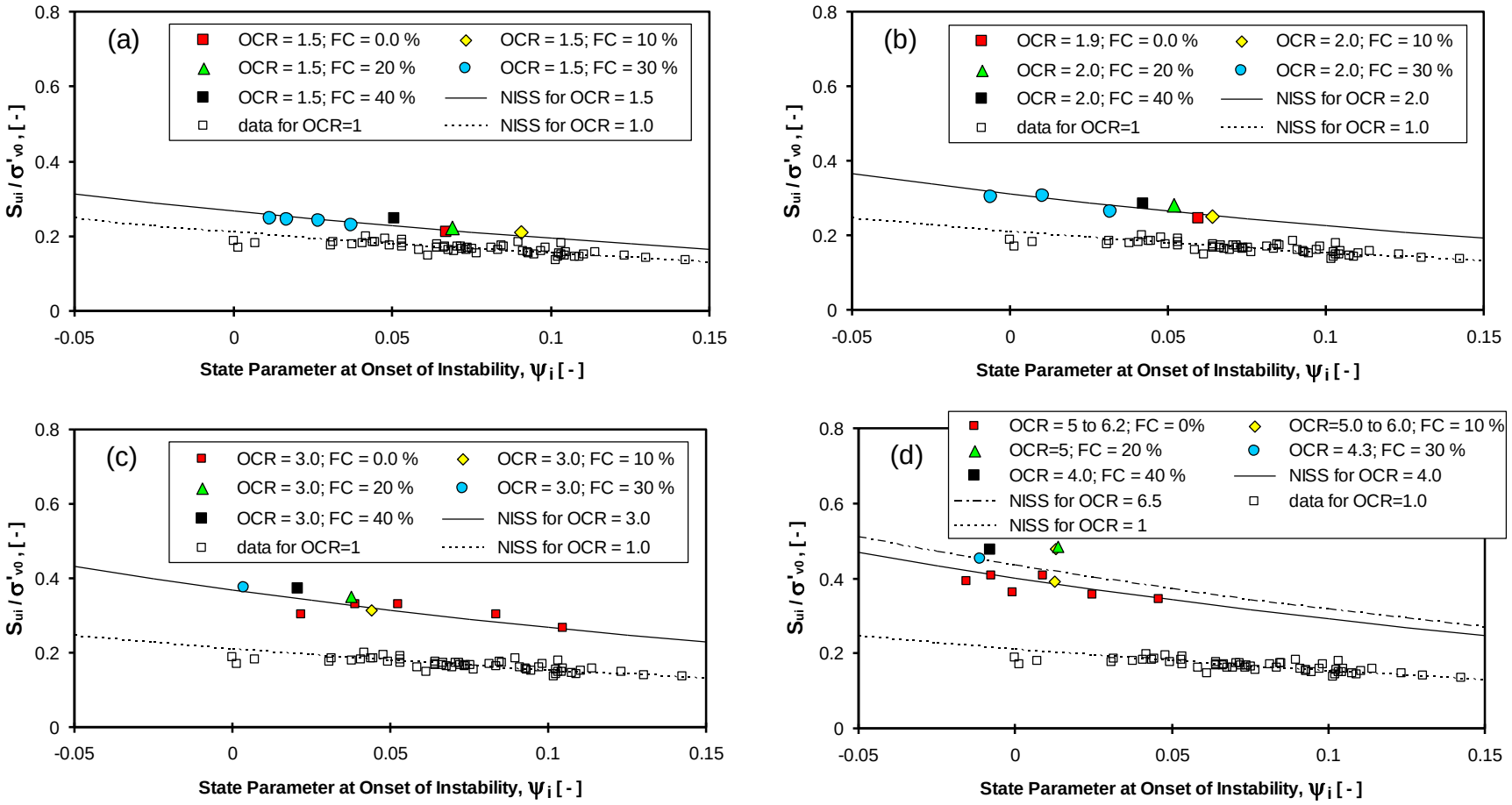


Fig. 10. Variation of Normalized Instability Shear Strength (NISS) in normally and over-consolidated Firoozkuh sand specimens for: (a) OCR=1.5, (b) OCR=2.0, (c) OCR=3.0, (d) OCR=4.0 to 6.2

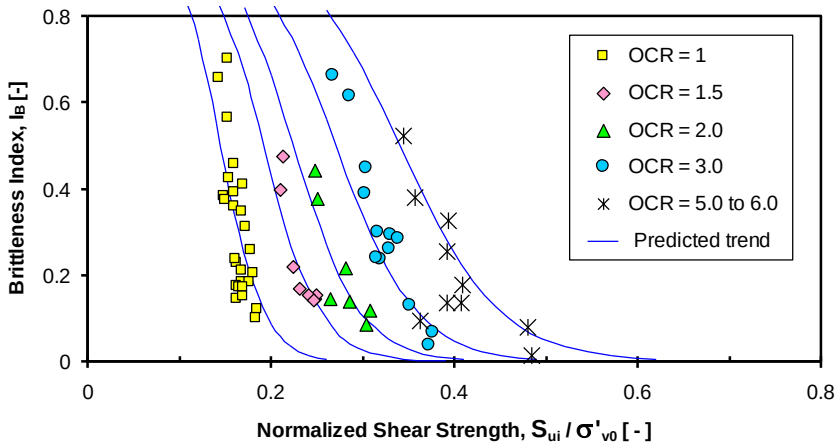


Fig. 11. Laboratory data and predicted curves for variation of brittleness index with normalized shear strength at the onset of instability for OCR=1.0, 1.5, 2.0, 3.0, and 5.0 to 6

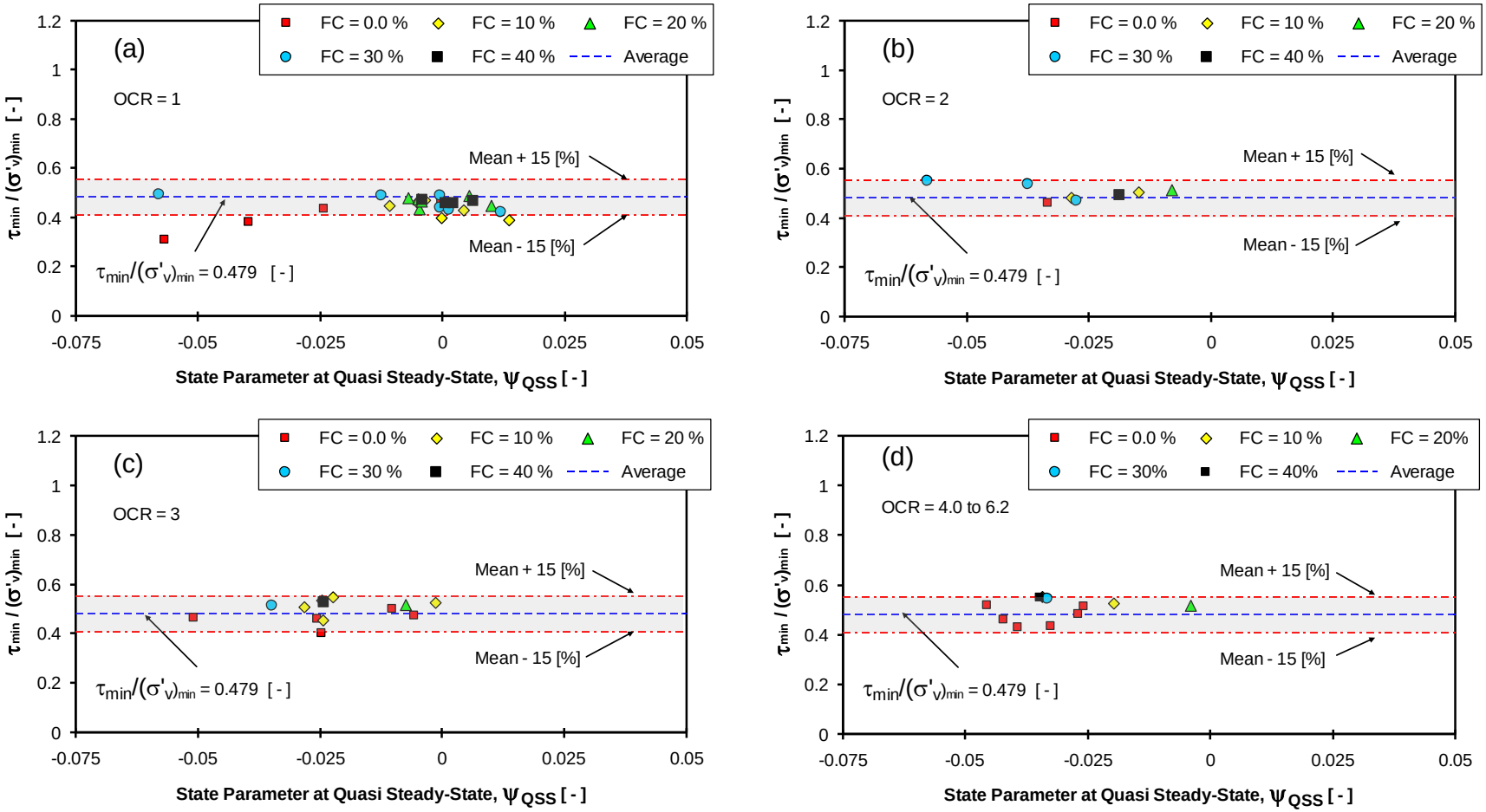


Fig. 12. Variation of $\frac{\tau_{min}}{(\sigma'_v)_{min}}$ for normally and over-consolidated Firoozkuh sand specimens with FC=0% to 40%: (a) OCR=1, (b) OCR=2.0, (c) OCR=3.0, and (d) OCR=5.0 to 6.2

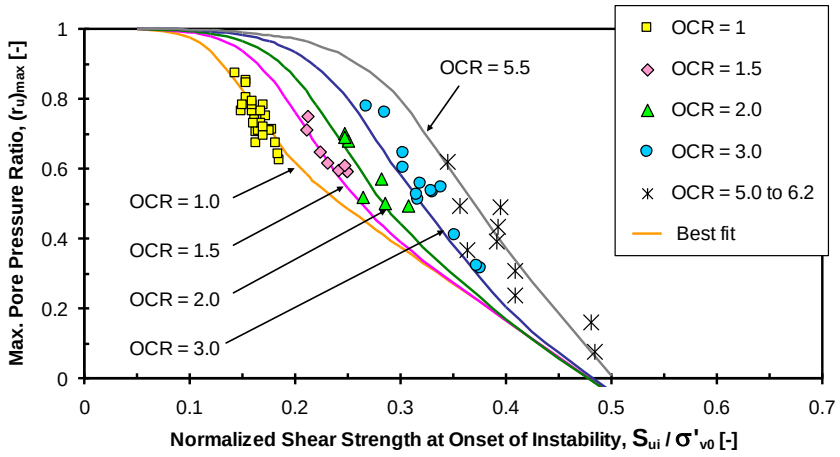


Fig. 13. Variation of the maximum normalized excess pore-water pressure [i.e., $(r_u)_{max} = \frac{\Delta u_{max}}{\sigma'_{v0}}$] with normalized shear strength at onset of instability for OCR=1.0, 1.5, 2.0, 3.0, and 5.0 to 6.2